Chapter 8

Calibration of Time Projection Chambers

Calibrating the Time Projection Chamber (TPC) is a crucial step to study and correct for physics processes and detector effects impacting the deposited charges on wire planes. Key processes affecting the production, propagation and detection of ionisation electrons were detailed in Chapter 3, of which electron attenuation and recombination are discussed in this chapter. Both these processes have been well-studied by other LArTPC experiments like MicroBooNE [1, 2], ArgoNeuT [3], and ICARUS [4, 5]. Their results have demonstrated an improvement in the spatial, temporal, and energy resolution of charge signals after correcting for these effects, illustrating the importance of calibration to achieve high precision measurements.

Two MC studies within the scope of charge calibration are presented in this chapter. The first study is presented in Sec. 8.1, focusing on electron lifetime measurement. Details of the second study are provided in Sec. 8.2, including an assessment of the impacts of delta ray fluctuations on recombination. Sec. 8.3 concludes the chapter with some remarks.

8.1 Electron Lifetime Measurement

Drifting electrons can be captured by electronegative impurities present in liquid argon, as previously described in Sec. 3.3.1. The reduction of the number of charges collected on a wire can be modelled as an exponential decay function following Eq. 3.6, where the electron lifetime τ indicates the purity level of the detector. A higher electron lifetime corresponds to a higher purity and vice versa. The electron lifetime can be precisely measured and used to recover the original charge deposition on the wires.

At SBND, there are several methods to measure the electron lifetime. Firstly, three purity monitors were installed, two inside the cryostat and one outside, which provide quick and real-time monitoring of the purity. Another method requires a dedicated extraction of electron lifetime using deposited charges as measured by the wires. This calibration procedure is often performed on a sample of cosmic muons that fully cross the drift distance of the TPC, known as *anode-to-cathode* cosmic tracks. Since they traverse the whole drift distance, they make a good sample to study the charge per unit length dQ/dx dependency on the drift distance. The MicroBooNE experiment also employed the same anode-to-cathode-crossing cosmic tracks for their electron lifetime measurement and demonstrated an excellent energy scale uncertainty post-calibration [1].

The study aims to develop a procedure to measure electron lifetime and investigate detector effects that can introduce biases on the lifetime, such as diffusion and Space Charge Effect (SCE). Within the scope of this study, MC samples of crossing cosmic tracks were simulated to perform the lifetime measurement. The procedure for electron lifetime measurement is outlined in Sec. 8.1.1, followed by Sec. 8.1.2 describing biases in lifetime measurement due to detector effects.

8.1.1 Electron Lifetime Extraction Procedure

The electron lifetime measurement requires information on the charge per unit length dQ/dx and the respective drift time t_{drift} of that charge cluster arrived at the wire. The charge reconstruction follows the workflow described in Sec. 6.2, whilst additional calculation is required to deduce the drift time. The drift time is defined as

$$t_{drift} = \frac{x}{v_d} \tag{8.1}$$

where x is the position of the charge deposition in drift direction (x-axis) and v_d is the drift velocity. At SBND, the drift velocity is expected to be at 0.1563 cm/μs at an electric field of 0.5

kV/cm and temperature of 88.4 K. The drift time can be calculated using the time recorded by the TPC readout when a charge cluster arrives at a wire t_m which is defined as [6]

$$t_m = t_0 - t_{trigger} + t_{drift} \tag{8.2}$$

where t_0 is the time when the particle enters the detector and $t_{trigger}$ is the time when the TPC readout is triggered. For a beam neutrino that triggers the TPC readout, the readout window is configured to align with when the beam arrives at the detector such that $t_{trigger} = t_0$, as illustrated in Fig. 4.8 in Sec. 4.2.7. On the other hand, a cosmic muon can occur anytime within the readout window, and the time when it enters the detector t_0 is unknown.

A *cathode stitching* process was developed by the ProtoDUNE and Pandora collaboration to determine the t_0 of cosmic muons that cross the cathode [6]. This can be applied to any LArTPC experiments that have two TPCs sharing the same cathode. Fig. 8.1 depicts the *stitching* process. Two cosmic track segments, shown by the red and blue lines, were reconstructed under an initial assumption of $t_0 = 0$, and thus, they appear at the wrong positions in both drift volumes. The reconstruction algorithm then shifts the drift coordinate in each TPC by an equal and opposite amount until the two segments are *stitched* at the cathode, shown by the black line, recovering the correct t_0. This method has been implemented in the reconstruction workflow of SBND, and it was applied to reconstruct the sample of anode-to-cathode-crossing tracks in this study.
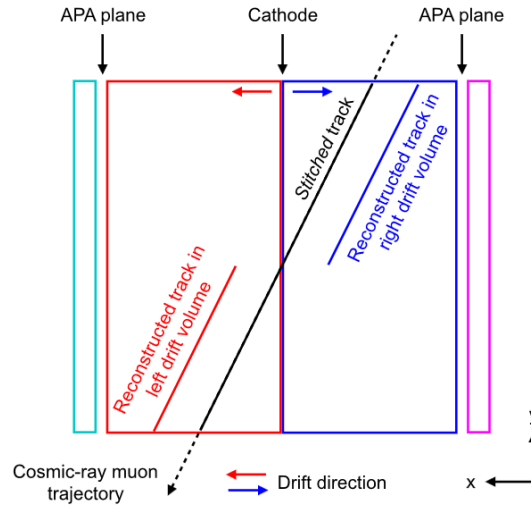

Fig. 8.1 Diagram depicting the cathode stictching process to determine the t_0 of cathode-crossing track [6].

The next step in the lifetime extraction procedure was to plot the charge per unit length dQ/dx in bins of the drift time t_{drift}. Fig. 8.2 shows an example dQ/dx profile in the drift time bin from 0.925 to 0.95 ms. A Landau-Gaussian convolution is fitted to the profile to extract the Most Probable Value (MPV) of dQ/dx [7]. This process was repeated for every drift time bin across the full drift distance of the TPC. Fig. 8.3 shows the MPV dQ/dx as a function of drift time, for TPC 0 (east) and 1 (west) of SBND. Bins of drift time less than 0.25 ms and larger than 1.15 ms were excluded due to the close proximity to the anode and cathode respectively, which can introduce some boundary effects. The MPV dQ/dx distribution is fitted with Eq. 3.6 to determine the electron lifetime constant. The MC sample input to Fig. 8.3 was simulated with a lifetime of 10 ms and no detector effects enabled to validate the procedure. The lifetimes were determined to be 10.12 and 10.40 ms, for TPC 0 and 1 respectively, showing a good agreement between the result and the simulation.
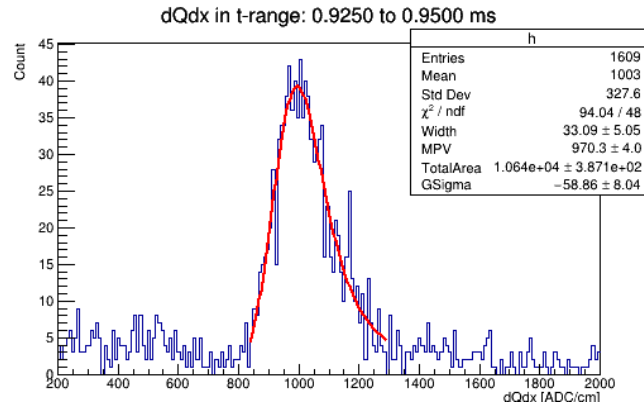

Fig. 8.2 Example of a dQ/dx profile in a drift time bin of 0.925–0.95 ms, fitted with a Landau-Gaussian convolution.
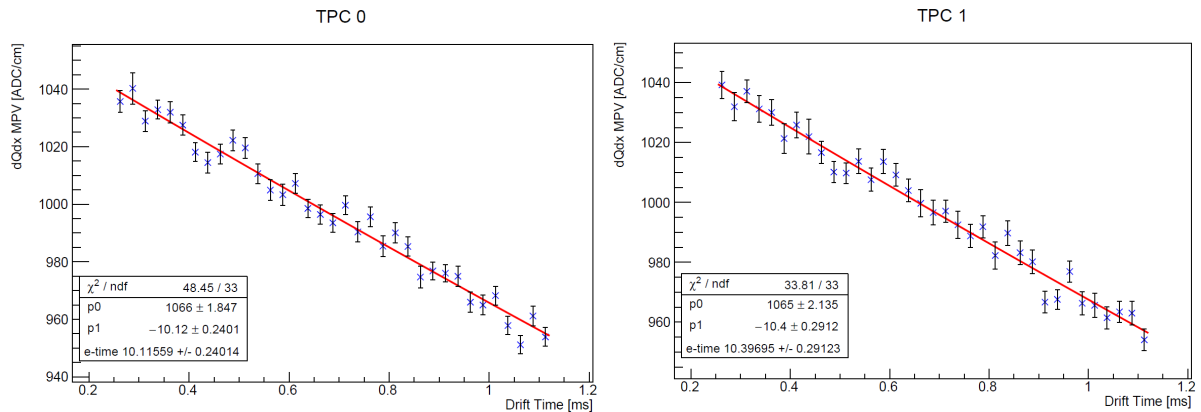

Fig. 8.3 MPV dQ/dx as a function of drift time, fitted with an exponential function.

106

8.1.2   Bias Study From Diffusion and Space Charge Effects

Some detector effects can introduce biases to the electron lifetime measurement, specifically those that can influence the propagation path of drifting electrons such as diffusion and SCE. Diffusion can smear both spatial and temporal resolution of the drifting electrons, and consequently the number of wires seen by the charge and the arrival time of charge measured by the wires. Meanwhile, SCE impacts both the amplitude of the measured charge as well as the temporal and spatial resolution due to electric field distortion. In view of this, a study was undertaken to understand how each effect introduces biases to the measurement of electron lifetime.

Three dedicated MC samples were simulated: (1) No SCE nor diffusion enabled, (2) only diffusion enabled and (3) only SCE enabled. In the diffusion-only MC sample, the longitudinal diffusion coefficient was set at $D_L = 4.0$ cm^2/s, as measured by MicroBooNE [8], and the transverse diffusion coefficient was set at $D_T = 8.8$ cm^2/s, as measured by ProtoDUNE [9]. In the SCE-only MC sample, the simulation of electric field distortion follows the description in Ref. [10].

Biases in the lifetime compared to the simulated lifetime are shown in Fig. 8.4, for two simulated electron lifetimes at 3 ms (top) and 10 ms (bottom). When no detector effects are enabled in the simulation, the determined lifetimes are very similar to the simulated lifetimes. At both simulated values of electron lifetimes, the observed biases are well below the 2% level. When either diffusion or SCE was enabled in the simulation, biases in the lifetimes can be seen. Biases due to diffusion only are at ~ 2% and ~ 8% for the simulated lifetimes of 3 ms and 10 ms respectively. On the other hand, biases due to SCE only are at ~ 5% and ~ 22% at the 3 ms and 10 ms lifetime. The observed biases are also consistent across the two TPC volumes of SBND.

The first observation is that the magnitude of the biases due to SCE is much greater than due to diffusion at both simulated lifetimes. This is consistent with the observations from an electron lifetime measurement carried out by MicroBooNE [2]. The paper demonstrated that both SCE and the transverse component of diffusion cause biases in the lifetime, however, biases due to transverse diffusion are smaller in magnitude than SCE. The paper also pointed out that the longitudinal component of diffusion causes insignificant biases in the lifetime. The second observation is that the longer the lifetime, the larger the biases as compared between the lifetimes at 3 ms and 10 ms. This is due to more drifting electrons surviving with a larger lifetime and thus, becoming more susceptible to detector effects.
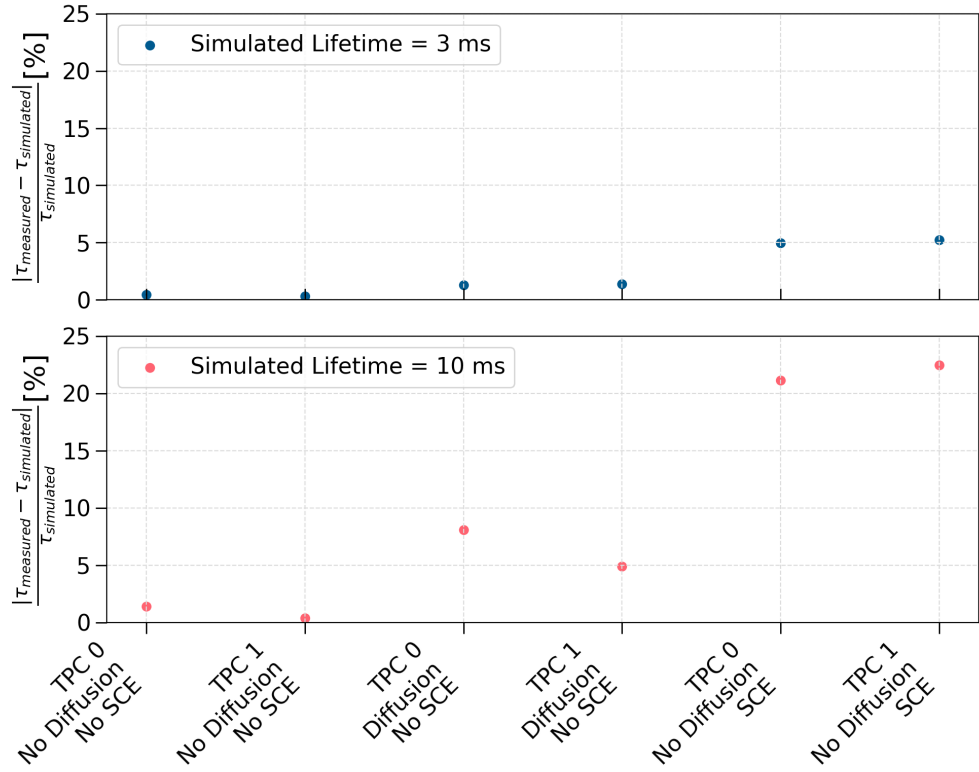
Fig. 8.4 Biases in electron lifetimes compared to the simulated values at 3 ms (top) and 10 ms (bottom).

Since the results of this study, an investigation carried out by Putnam and Schmitz at the ICARUS experiment demonstrated that transverse diffusion breaks down the Landau-Gaussian MPV approximation of the measured charge [5], which was employed in this study. This is due to transverse diffusion smearing the charge cluster across multiple wires. The paper recommends using an averaged dQ/dx from a group of wires instead of dQ/dx from a single wire to mitigate the effect. The suggestion has now been implemented at SBND.

The study presented here demonstrates a method to measure electron lifetime using a sample of anode-to-cathode crossing cosmic tracks. These tracks have the advantage of spanning over a full drift distance and a reconstructable t_0 time tagging when the particle enters the detector. The electron lifetime measured by this method is the most affected by SCE, followed by diffusion, which is consistent with the results from MicroBooNE. This procedure has now been replicated in preparation for the calibration run of SBND at the time of writing. A trigger requiring coincidence in the east and west CRT wall was deployed to produce dedicated samples containing crossing cosmic muon tracks that can be used for electron lifetime measurement.

8.2 Delta Ray Fluctuations on Recombination Simulation

Following the lifetime measurement, the next discussion focuses on recombination, a physics process that drives the charge and light yield as previously described in Sec. 3.2.3. SBND currently employs the Modified Box (ModBox) model for simulating recombination, with experimentally-derived parameters from ArgoNeuT [3]. The model approximates the recombination probability based on a cylindrical column surrounding a track-like charge deposition, effectively accounting for microphysics processes along the track. This approximation has proven to work well for the MeV to GeV-scale interactions, however, it breaks down at the keV-scale. Szydagis et al pointed out non-linear fluctuations in recombination at increasingly smaller scales that are not well-described by the ModBox model [11]. Moreover, the ArgoNeuT collaboration also proposed that microphysics effects could lead to disagreements in recombination theory, simulation and measurement [3].

One microphysics process that can affect recombination, highlighted by both Szydagis et al [11] and ArgoNeuT [3], is the production of delta rays. They are knock-out electrons with low energy but high energy per unit length dE/dx. As shown in Fig. 8.5, delta rays are short tracks produced along a longer primary track, in this case, a cosmic muon. Due to their high dE/dx, they are associated with a smaller recombination factor, producing more scintillation photons while reducing ionisation electrons.

This study is motivated to examine how the fluctuation in delta rays impacts the simulation of recombination, and consequently, the energy charge scales of different particle types. Sec. 8.2.1 provides an overview of the simulation framework of delta rays and recombination, and some concerns with the current framework. Sec. 8.2.2 and 8.2.3 describe the impacts of delta rays on the recombination magnitude and smearing respectively. Sec. 8.2.4 summarises some relevant studies of recombination carried out by the ICARUS collaboration.
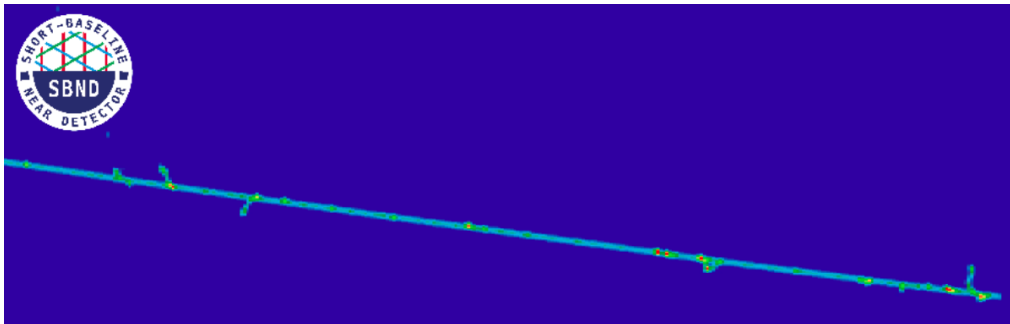

Fig. 8.5 Event display of a simulated cosmic muon track segment, with many delta rays produced along the primary track.

8.2.1   Simulation of Delta Rays and Recombination

The simulation of delta rays and recombination is part of the simulation of particle propagation from creation to detection point performed by the Geant4 toolkit [12], with the description provided in Sec. 5.4.1. The simulation propagates the primary particle step by step and applies physics processes at each step of length dx. Energy loss due to ionisation is simulated as two intertwined processes: (1) a continuous energy loss dE of the primary particle along the step dx and (2) a discrete energy loss dE at the end o f the step producing delta rays [12].

The continuous energy loss of the primary particle is simulated by Geant4 using complementary models depending on the energy range and particle charge [13]. The Bethe-Bloch formalism [7], detailed in Sec. 3.2.1, is used to compute dE/dx in the high energy range (> 2 MeV), and the free electron gas model is applied at the low energy range (< 1 keV for protons). In the intermediate range, parameterised models based on data from Ziegler [14] and ICRU [15] are implemented.

The total cross section of the delta ray production is computed using a user-defined energy threshold. The energy threshold defines the lower limit of the kinetic energy of delta rays so that only delta rays with sufficient energy can be produced. This is to suppress the simulation of all low energy delta rays that would exhaust computation resources. This also means that the energy of the non-produced delta rays is transferred to the continuous energy loss of the primary particle. This is equivalent to setting the energy threshold as the upper limit for the primary particle so that its mean continuous energy loss is less than the threshold. In other words, the energy threshold determines how much energy deposition is shared between the primary particle and the delta rays. The lower the threshold, the more energy deposition is carried away by the delta rays instead of the primary particle.

In Geant4 terminology, this energy threshold is also known as the secondary production threshold, where the minimum kinetic energy requirement for delta ray production is defined as the minimum distance the generated delta ray must be able to traverse in a given material. In the simulation framework of SBND, the secondary production threshold for delta rays in liquid argon is set as 700 μm, equivalent to having a kinetic energy of 273 keV. Moreover, the maximum length dx that the particle can propagate per step is configured as 0.3 mm, one order of magnitude smaller than the wire pitch of 3 mm. This setup allows for a feasible computation of generating delta rays.

For each step dx, the number of electron-ion pairs is calculated by dividing the continuous energy loss dE by the ionisation work function of argon W_{ion} = 23.6 eV [16]. Then,

the recombination factor R is applied to the number of electron-ion pairs according to the charge-light anti-correlation described by Eq. 3.2 and 3.3, to determine the final charge and light yield resulting from the step dx. Using the ModBox formalism, R is computed as [3]

$$R = \frac{\log\left(\alpha + \left(\beta \cdot dE/dx\right)/\varepsilon\right)}{\left(\beta \cdot dE/dx\right)/\varepsilon} \tag{8.3}$$

where ε (kV/cm) is the electric field at the position of the step, dE/dx (MeV/cm) is the energy per unit length, and parameters $\alpha = 0.93 \pm 0.02$ and $\beta = 0.212 \pm 0.002$ (kV/cm)(g/cm^2)/MeV were experimentally derived by ArgoNeuT [3]. Eq. 8.3 was shown earlier in Fig. 3.6, illustrating R as a function of dE/dx. It is important to note that R is dependent on the electric field and therefore can be influenced by local distortions of the field.

The simulation of delta rays and recombination described here gives rise to some concerns. The first concern is the assumption of a *universal* recombination factor R. The parameters α and β were measured by ArgoNeuT using a stopping proton sample, and wire planes with a pitch of 3 mm [3]. Nonetheless, they are applied to any type of ionising particles, which can influence the local ionisation density differently. Secondly, the secondary production threshold on delta rays removes low energy electrons in simulation. However, they are produced in reality and can fluctuate recombination at a local scale.

The study was set up to address the individual concerns outlined above to better understand their impacts on recombination. Identical MC samples of muons and protons were simulated to investigate if recombination is particle-dependent. The particles were generated with a fixed energy of 1 GeV, uniform in positional and angular distributions. The Geant4 simulation was configured such that the particle can only deposit energy via ionisation. The *true* energy per unit length dE/dx was computed from the *true* number of electrons per unit length dQ/dx, where *true* indicates no detector simulations were applied. The computation follows the energy-charge scale defined by the ModBox model as [3]

$$\frac{dE}{dx} = \frac{1}{\beta}\left[\exp\left(\beta W_{ion}\frac{dQ}{dx}\right) - \alpha\right] \tag{8.4}$$

where parameters are the same as Eq. 8.3. For each particle type, a range of secondary production thresholds of delta rays were simulated. The largest value, and also the current value being used by SBND, was set at 700 μm, equivalent to delta rays with a minimum kinetic energy of 273 keV. The smallest threshold was 1 μm, enabling the simulation of delta rays with kinetic energy as low as 1 keV. This variation was chosen to study the impacts due to delta ray fluctuations.

8.2.2 Impacts of Delta Ray Fluctuations On Recombination Magnitude

Fig. 8.6 shows the energy-charge scale, dQ/dx to dE/dx, for protons at the secondary production threshold at 700 μm and 1 μm. The calorimetry distribution is plotted for the proton residual range from 1 cm to 90 cm, which covers the full track length. The proton dE/dx ranges from 2 MeV/cm to 18 MeV/cm, allowing for the examination of delta ray fluctuation impacts at both low and high parts of the dE/dx spectrum. For the secondary production threshold of 700 μm, shown in Fig. 8.6a, the distribution precisely follows the ModBox model with the ArgoNeuT parameters defined in Eq. 8.4. Good agreement is expected since the simulation of SBND is similar to that of ArgoNeuT [3].

However, for the secondary production threshold of 1 μm, shown in Fig. 8.6b, deviations away from the ModBox model occur, such that the energy-charge scale shifts at both low and high parts of the dE/dx specturm. Lowering the secondary production threshold leads to more energy deposition carried by the delta rays instead of the primary proton, and thus, delta rays have a greater influence on recombination. At the low dE/dx spectrum of the proton, delta rays have higher dE/dx than that of the proton, and therefore a smaller recombination factor. This results in the *effective recombination factor* being reduced, decreasing dQ/dx at the same value of dE/dx. The opposite effect is seen at the high dE/dx spectrum of the proton, where dQ/dx is higher than the ModBox model. This indicates that the effective recombination factor increases.

The proton energy-charge scale at the secondary production thresholds at 700, 10, 5, and 1 μm, equivalent to delta rays with a minimum kinetic energy of 272.58, 14.60, 2.58, 1.06, and 0.99 keV are plotted in Fig. 8.7. To compare dQ/dx quantitatively at the same dE/dx bin, the
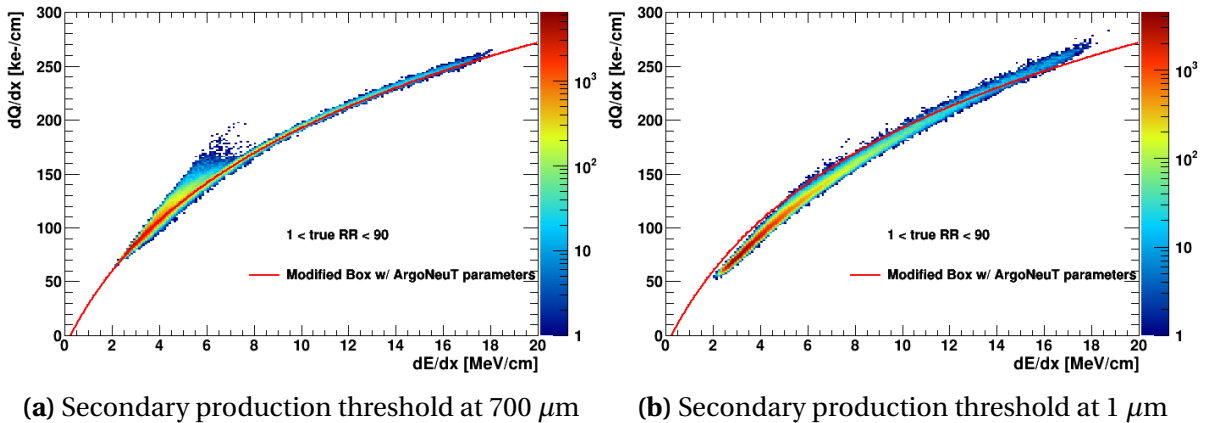

(a) Secondary production threshold at 700 μm   **(b)** Secondary production threshold at 1 μm

Fig. 8.6 dQ/dx as a function of dE/dx for a 1 GeV proton at the secondary production threshold of (a) 700 μm and (b) 1 μm.

mean dQ/dx is calculated per dE/dx bin as shown in Fig. 8.7a. The percentage difference of the mean dQ/dx relative to the ModBox model is plotted in Fig. 8.7b to quantify the magnitude of the differences.

Lowering the kinetic energy of delta rays results in two key trends. Firstly, the dE/dx position at which the proton energy-charge scale shifts in upward/downward directions, increases with lower delta ray kinetic energy. This shift position can be seen in Fig. 8.7b. Secondly, the magnitude of the deviations depends on the secondary production threshold. At low dE/dx, the effective recombination is reduced the most for the secondary production threshold set as 1 μm, as shown in yellow. At high dE/dx, the effective recombination is the highest for the secondary production threshold set as 5 μm, as shown in green. This is evidence that delta ray fluctuations can greatly influence the proton energy-charge scale. The more energy loss is carried away by delta rays, especially by those with very low kinetic energy, the more distorted the energy-charge scale becomes.
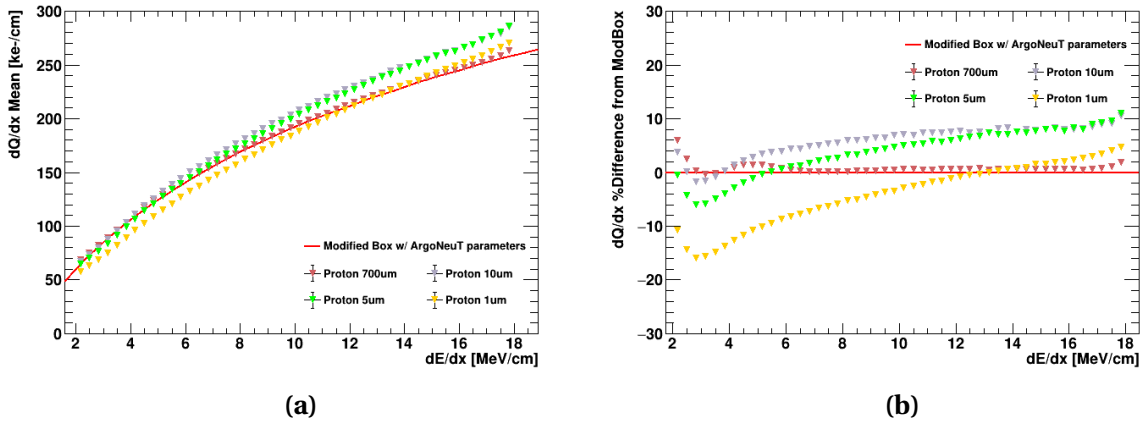

Fig. 8.7 (a) Mean dQ/dx and (b) its percentage difference relative to the Mod-Box model as a function of dE/dx for a 1 GeV proton.

The energy-charge scale for muons is plotted in Fig. 8.8, for the secondary production threshold at 700 μm and 1 μm. Fig. 8.8a and 8.8b contain the full muon residual range, covering the track length 1–400 cm. Two distinct distributions can be seen here, one linear from the Minimum Ionising Particle (MIP) region, and another one that follows the ModBox model indicating the stopping region. The linear energy-charge scale has been well-observed with MIP muons [1]. To examine the stopping region exclusively, a residual range requirement of less than 10 cm was applied, as shown in Fig. 8.8c and 8.8d. Some remnants from the MIP region can still be seen in the dE/dx range between 4 to 12 MeV/cm. Comparing Fig. 8.8c and 8.8d shows the same behaviour as protons at the same low dE/dx range, delta rays with lower kinetic energy result in a smaller effective recombination factor.

113

The mean dQ/dx of muons and its percentage difference relative to the ModBox model are also plotted as shown in Fig. 8.9, at various values of the secondary production thresholds. Similar to protons, the magnitude of the effective recombination reduction increases with lower delta ray kinetic energy. The recombination factor is also the most affected at the secondary production threshold of 1 μm, as shown in red. It is also important to note that the magnitude of the reduction is larger for muons compared to protons, which is likely due to the amount of delta rays produced by each particle type. For instance, at the same dE/dx of 3 MeV/cm and the secondary production threshold of 1 μm, the percentage difference is at ∼ 24% for muons and ∼ 16% for protons.

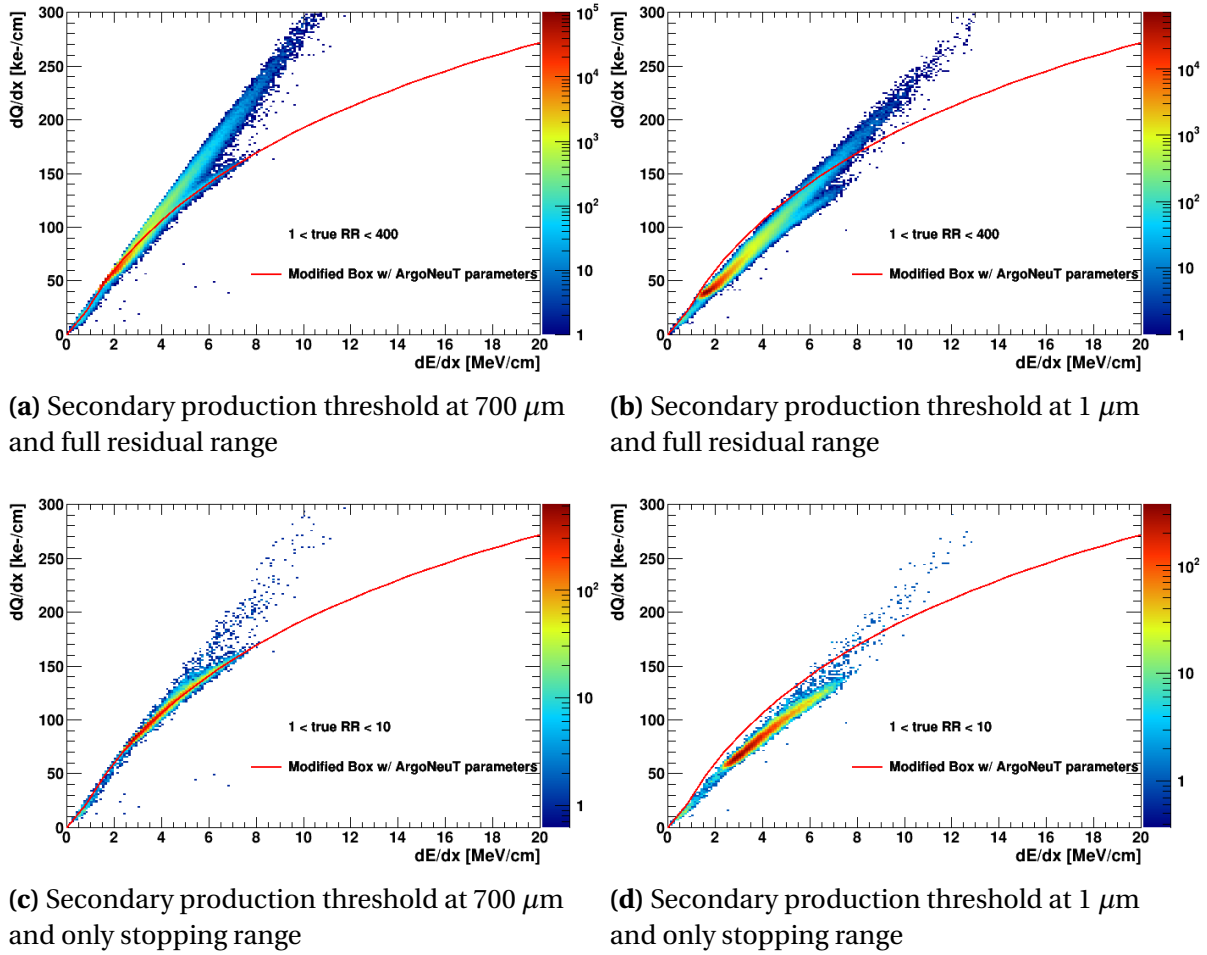**(a)** Secondary production threshold at 700 μm and full residual range

(b) Secondary production threshold at 1 μm and full residual range

(c) Secondary production threshold at 700 μm and only stopping range

(d) Secondary production threshold at 1 μm and only stopping range

Fig. 8.8 dQ/dx as a function of dE/dx for a 1 GeV muon at the secondary production threshold of 700 μm (left) and 1 μm (right) and for the full residual range (top) and only the stopping range (bottom).
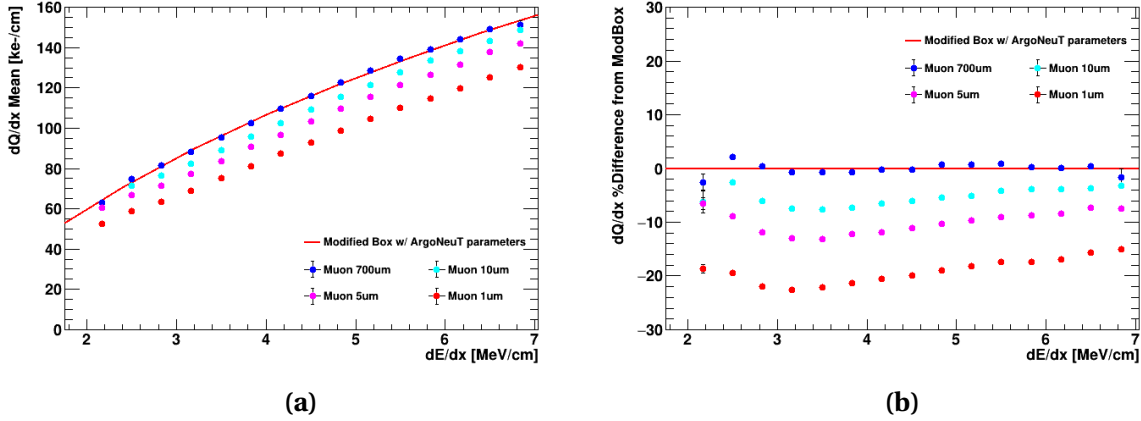
Fig. 8.9 (a) Mean dQ/dx and (b) its percentage difference relative to the Mod-Box model as a function of dE/dx for a 1 GeV muon.

8.2.3   Impacts of Delta Ray Fluctuations On Recombination Smearing

The effects of delta rays on recombination also extend to smearing of the energy-charge scale. To disentangle how the Geant4 toolkit handles the smearing due to delta rays, an additional study was carried out in which the energy deposition of the primary particle was isolated from delta rays.

Fig. 8.10 shows the dE/dx of the primary proton as a function of its residual range, compared against the Landau-Vavilov distribution [7]. Energy loss due to delta rays is included in the top two plots, Fig. 8.10a and Fig. 8.10b, for the secondary production thresholds of 700 μm and 1 μm. Meanwhile, the bottom two plots, Fig. 8.10c and Fig. 8.10d, only include the energy loss the primary proton. The same set of plots are also computed for the case of muons as shown in Fig. 8.11.

When delta rays are included in the energy deposition, the dE/dx distribution agrees with the Landau-Vavilov distribution with some smearing in dE/dx across all bins of the residual range. The energy distributions are indistinguishable between the secondary production threshold of 700 μm and 1 μm. This can be seen for both protons, comparing Fig. 8.10a and Fig. 8.10b, and muons, comparing Fig. 8.11a and 8.11b. The behaviour is expected since the total energy deposition of the primary particle and the delta rays must stay the same regardless of the secondary production threshold. Comparing the protons and muons, including delta rays in the total energy deposition introduces greater smearing in the dE/dx distribution for muons than protons.
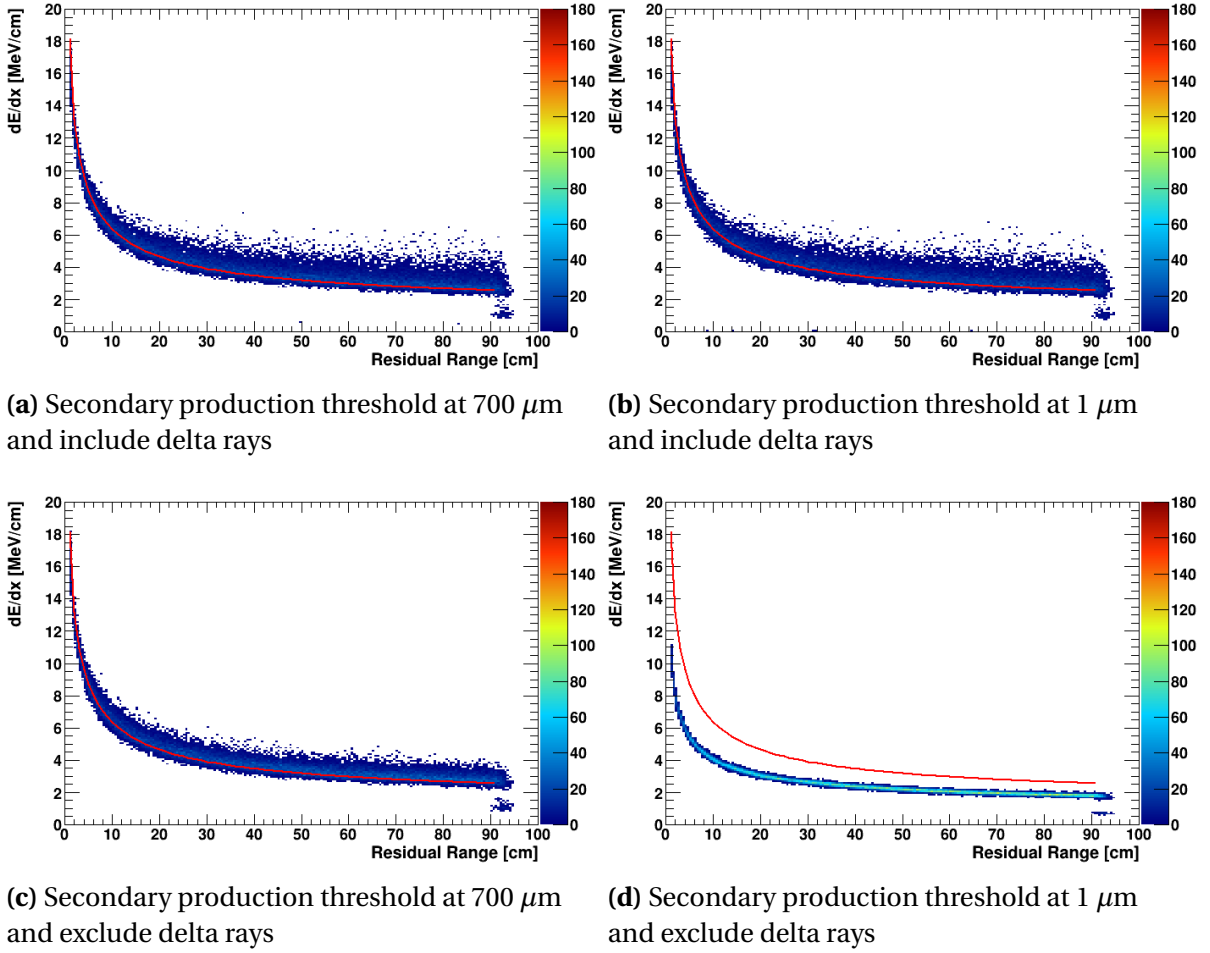
(a) Secondary production threshold at 700 μm and include delta rays

(b) Secondary production threshold at 1 μm and include delta rays

(c) Secondary production threshold at 700 μm and exclude delta rays

(d) Secondary production threshold at 1 μm and exclude delta rays

Fig. 8.10 dE/dx as a function of residual range for a 1 GeV proton at the secondary production threshold of 700 μm (left) and 1 μm (right), including (top) and excluding (bottom) the energy loss due to delta rays.

When delta rays are excluded in the distribution of the energy loss, some noticeable effects can be seen. At the secondary production threshold at 700 μm, the dE/dx distribution of only the primary particle still follows closely the Landau-Vavilov distribution. However, it contains less smearing in dE/dx compared to when delta rays are included in the energy loss. This can be seen comparing Fig. 8.10a and Fig. 8.10c for protons, and comparing Fig. 8.11a and 8.11c for muons. At this configuration, the majority of the energy deposition is carried away by the primary particle, and Geant4 already accounts for delta ray fluctuations when sampling the mean energy loss of the primary particle [12]. Introducing energy loss by delta rays only adds some additional smearing to the total dE/dx distribution.

(a) Secondary production threshold at 700 μm and include delta rays

(b) Secondary production threshold at 1 μm and include delta rays

(c) Secondary production threshold at 700 μm and exclude delta rays

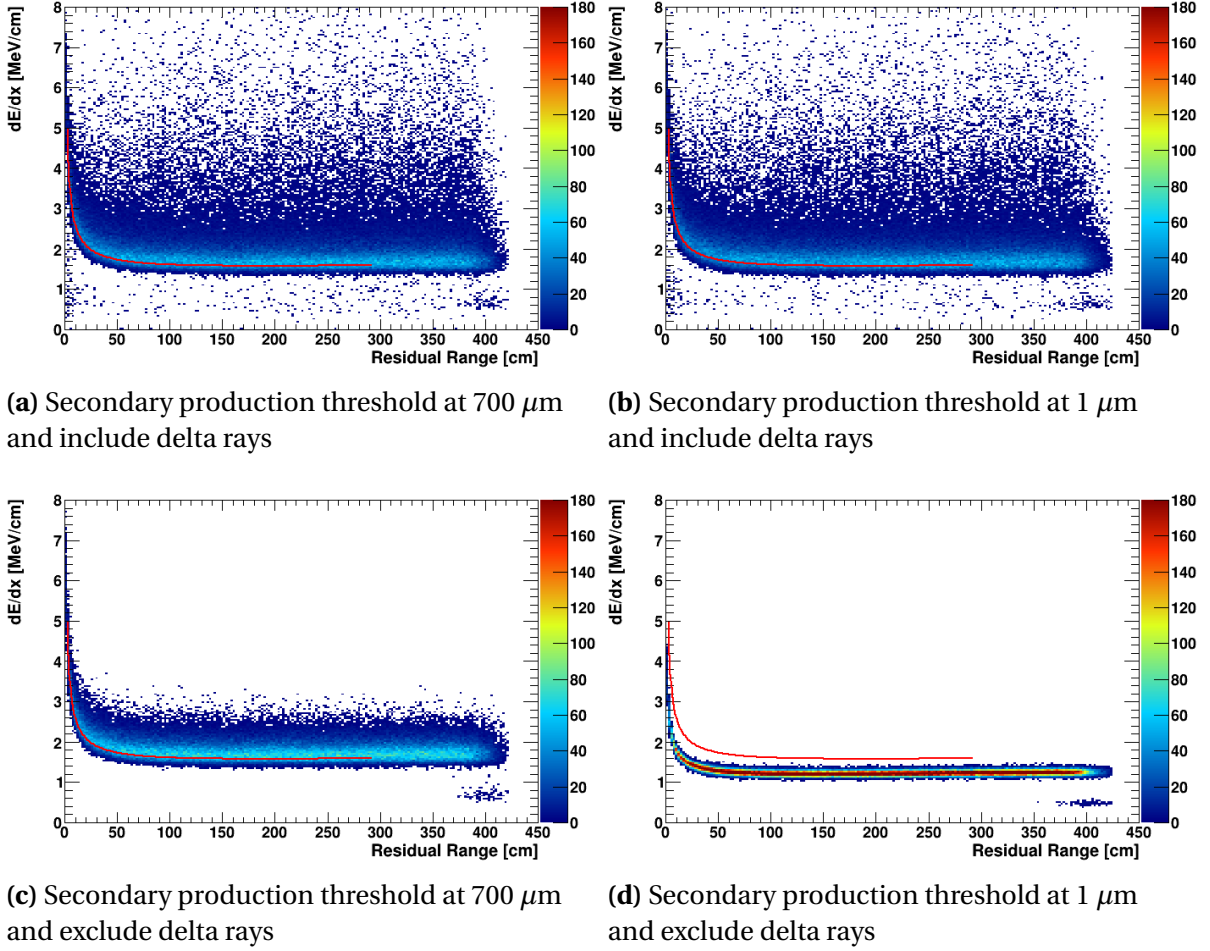**(d)** Secondary production threshold at 1 μm and exclude delta rays

Fig. 8.11 dE/dx as a function of residual range for a 1 GeV muon at the secondary production threshold of 700 μm (left) and 1 μm (right), including (top) and excluding (bottom) the energy loss due to delta rays.

On the other hand, when the secondary production threshold is set to 1 μm and no delta rays are considered, the dE/dx distribution of only the primary particle becomes narrow without any smearing and fails to follow the Landau-Vavilov distribution. This can be seen in Fig. 8.10d for protons and Fig. 8.11d for muons. Isolating only the energy deposition of the primary particle is equivalent to observing a *bare* proton or muon track without any delta rays produced along its path, which has not been experimentally measured before. In this case, the stopping power distribution of the primary particle is computed by Geant4 using interpolation instead of using data-based parametrisation [12]. This potentially leads to inaccuracy in simulating the energy loss due to ionisation.

The study here demonstrates that fluctuations of delta rays can introduce different effects on recombination. Firstly, delta rays have a different dE/dx compared to the primary particle and therefore, can influence the effective recombination factor. At the low end of the dE/dx spectrum of the primary particle, this results in an overall reduction of recombination. Meanwhile, at the high end of the dE/dx spectrum, they can increase the effective recombination factor. This leads to a distortion of the observed energy-charge scale of a particle. Secondly, having a different dE/dx to the primary particle also means that delta rays can also smear the observed energy-charge scale. Finally, the magnitude of these impacts vary differently between protons and muons, suggesting a need for a particle-dependent recombination factor.

8.2.4   Recombination Studies From The ICARUS Experiment

A very similar study was carried out by the ICARUS collaboration in 2004 in Italy, to investigate delta ray fluctuations impacting recombination and also to compare against their experimental data [4]. The result is shown in Fig. 8.12, showing the recombination factor as a function of the delta ray secondary production threshold in MC. The dotted line is the expectation for a MIP muon with a kinetic energy of 250 MeV. The recombination factor increases with the threshold and peaks at ~ 0.7, then decreases with higher thresholds. This result is similar to the observation of the study described above, where the effective recombination factor reduces at small values of delta ray secondary production thresholds.
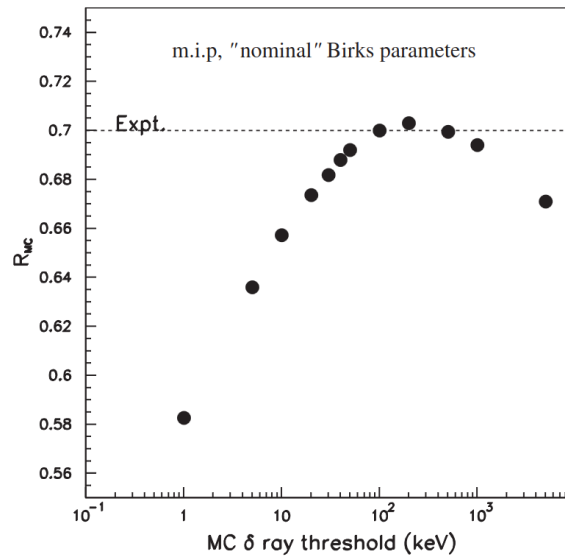

Fig. 8.12 Recombination factor as a function of the delta ray threshold [4].

The collaboration proposed a few different approaches toward the simulation recombination so that delta ray fluctuations can be more accurately simulated [4]. The first approach was to simulate *as microscopic as possible*, by simulating delta rays with kinetic energy $\mathcal{O}(1$ eV) and range $\mathcal{O}(10$ nm). However, they concluded that this approach was not feasible. Firstly, the effective recombination factor of a particle always contains effects due to delta rays, and secondly, computing resources are limited. Another proposal was an empirical approach, to choose the best secondary production threshold in simulation to reproduce the data with a reasonable computing consumption. This number was found to be 3 μm, equivalent to simulating delta rays having a kinetic energy as low as 10 keV.

Also recently from the ICARUS collaboration, now with the detector relocated to Fermilab, a study in 2024 of recombination showed a clear dependence of recombination on the angle of the particle track to the drift electric field [**TODO**]. A new ellipsoid modified box model of recombination was proposed and able to describe the data across all measured angles. This result has significantly improved the observed energy-charge scale of a particle, which is critical for particle identification of an LArTPC.

These results from the ICARUS collaboration have collectively enhanced the understanding of recombination, as well as guided how to model recombination at SBND. In the scope of calibrating the SBND detector, it is highly recommended to follow a data-driven approach such that the simulation of delta rays and recombination should be tuned to best match the observed data, as done by earlier experiments like ICARUS and ArgoNeuT.

8.3   Concluding Remarks

Two studies within the scope of calibrating ionisation electron signals were presented. The first study described a procedure to measure electron lifetime using anode-to-cathode crossing cosmic muons and quantify biases in the acquired lifetime due to SCE and diffusion. The second study examined the simulation of delta rays and recombination, and how delta ray fluctuations can impact the effective recombination factor and consequently, the energy-charge scale of a particle. These studies help understanding how different detector effects and physics processes can impact the charge depositions on wires, which can be pinned down and corrected for. This calibration process enables high precision measurements, which are essential for any physics analysis at SBND, including the search for HNLs. The following Chapter 9 will focus on the selection of HNLs, of which many reconstruction variables describing the calorimetry and topology of a particle relies on having an accurate charge information.

References

[1] C. Adams et al. (MicroBooNE), "Calibration of the charge and energy loss per unit length of the MicroBooNE liquid argon time projection chamber using muons and protons", JINST **15**, P03022 (2020).

[2] R. Acciarri et al. (MicroBooNE,), "A Measurement of the Attenuation of Drifting Electrons in the MicroBooNE LArTPC", 10.2172/1573054 (2017).

[3] R. Acciarri et al., "A study of electron recombination using highly ionizing particles in the ArgoNeuT Liquid Argon TPC", Journal of Instrumentation **8**, P08005 (2013).

[4] S. Amoruso et al., "Study of electron recombination in liquid argon with the ICARUS TPC", Nuclear Instruments and Methods in Physics Research Section A: Accelerators, Spectrometers, Detectors and Associated Equipment **523**, 275–286 (2004).

[5] G. Putnam et al., "Effect of diffusion on the peak value of energy loss observed in a LArTPC", JINST **17**, P10044 (2022).

[6] A. A. Abud et al. (DUNE Collaboration), "Reconstruction of interactions in the ProtoDUNE-SP detector with Pandora", The European Physical Journal C **83**, 618 (2023).

[7] D. E. Groom et al., "Passage of particles through matter", The European Physical Journal C - Particles and Fields **15**, 163–173 (2000).

[8] P. Abratenko et al. (MicroBooNE), "Measurement of the longitudinal diffusion of ionization electrons in the MicroBooNE detector", Journal of Instrumentation **16**, P09025 (2021).

[9] B. Abi et al., "First results on ProtoDUNE-SP liquid argon time projection chamber performance from a beam test at the CERN Neutrino Platform", Journal of Instrumentation **15**, P12004 (2020).

[10] M. Mooney, "The MicroBooNE Experiment and the Impact of Space Charge Effects", in Meeting of the APS Division of Particles and Fields (Nov. 2015).

[11] M. Szydagis et al., "A Review of Basic Energy Reconstruction Techniques in Liquid Xenon and Argon Detectors for Dark Matter and Neutrino Physics Using NEST", Instruments **5**, 13 (2021).

[12] S. Agostinelli et al., "Geant4—a simulation toolkit", Nuclear Instruments and Methods in Physics Research Section A: Accelerators, Spectrometers, Detectors and Associated Equipment **506**, 250–303 (2003).

[13] S. Giani et al., "GEANT4 simulation of energy losses of ions", (1999).

[14] H. H. Andersen et al., *Hydrogen Stopping powers and ranges in all elements* (Pergamon Press, United States, 1977).

[15] "ICRU Report 49, Stopping Power and Ranges for Protons and Alpha Particles", Journal of the ICRU **os-25** (1993).

[16] M. Miyajima et al., "Average energy expended per ion pair in liquid argon", Phys. Rev. A **9**, 1438–1443 (1974).